Deep-Sea Research I 57 (2010) 880–892

Contents lists available at ScienceDirect

Deep-Sea Research I

journal homepage: www.elsevier.com/locate/dsri

Larval dispersion along an axially symmetric mid-ocean ridge

D.J. McGillicuddy Jr.[a,*], J.W. Lavelle[b], A.M. Thurnherr[c], V.K. Kosnyrev[a], L.S. Mullineaux[d]

[a] Department of Applied Ocean Physics and Engineering, Woods Hole Oceanographic Institution, Woods Hole, MA 02543, USA
[b] NOAA/Pacific Marine Environmental Laboratory, 7600 Sand Point Way, N.E. Seattle, WA 98115, USA
[c] Lamont-Doherty Earth Observatory, Palisades, NY 10964, USA
[d] Biology Department, Woods Hole Oceanographic Institution, Woods Hole, MA 02543, USA

ARTICLE INFO

Article history:
Received 23 June 2009
Received in revised form
26 March 2010
Accepted 7 April 2010
Available online 10 April 2010

Keywords:
East Pacific Rise
Larval transport
Larval behavior
Modeling
Physical–biological interactions

ABSTRACT

We investigated planktonic larval transport processes along an axially symmetric mid-ocean ridge with characteristics similar to that of the East Pacific Rise (EPR) segment at 9–10°N. The hydrodynamic basis for this study is a primitive equation model implemented in two dimensions (depth and across-ridge), forced at the open boundaries to provide suitably realistic simulation of currents observed on the EPR ridge crest from May to November 1999. Three-dimensional trajectories of numerical larvae are computed assuming homogeneity in currents in the along-ridge direction. Larval dispersal fluctuates significantly in time. Transport distance decreases systematically with height above the bottom where numerical larvae are less subject to strong currents along the flanks of the ridge. The probability that the simulated larvae will be located near the ridge crest at settlement depends strongly on their behavioral characteristics (vertical position in the water column during the larval stage) and the length of their precompetency period.

© 2010 Elsevier Ltd. All rights reserved.

1. Introduction

For sessile organisms, a life cycle that includes a planktonic stage confers substantial opportunity for dispersal. Hydrodynamic transport of the larval stage is advantageous in terms of colonization of new areas, yet disadvantageous with respect to self-sustenance of local populations. Balance between the conflicting objectives of dispersal and retention is to some degree set by life history parameters (Strathmann, 1985). The maximum time an organism can survive in the planktonic larval stage is referred to as the *larval life span*. The initial time interval after spawning during which a larva is not fit to settle is referred to as the *precompetency period*. From the perspective of larval settlement success, minimization of the precompetency period and maximization of the larval life span provide the most flexibility in terms of dispersal and retention.

Benthic organisms inhabiting hydrothermal vent systems face particularly acute challenges with respect to survival of their planktonic larvae, insofar as areas of suitable substrate are quite limited in spatial extent, relatively few in number, and geographically isolated. Larvae of most hydrothermal vent species are small (Berg and Van Dover, 1987; Mullineaux et al., 1995) and appear to be relatively weak swimmers, suggesting that their dispersal may be determined largely by ocean currents. Planktonic larvae of the dominant vent species do not feed (Lutz et al., 1980; Tyler and Young, 1999). Similar species in shallow water environments have short larval life spans (hours to days). However, physiological studies of Antarctic asteroids have shown that non-feeding larvae may remain viable in the planktonic stage for months, due to lowered metabolism in cold water (Hoegh-Guldberg et al., 1991). The vent tubeworm *Riftia pachyptila* has been cultured to obtain direct estimates of life span (Marsh et al., 2001); the larvae can live on the order of 30–40 days without feeding. If the larvae are transported as passive neutrally buoyant particles, they have the potential to disperse distances on the order of 100 km in typical East Pacific Rise (EPR) flows (Mullineaux et al., 2002). Using measured currents, inferred larval life spans, and a dispersal model, Chevaldonné et al. (1997) suggested larvae of the vent polychaete *Alvinella* should be able to traverse the distances necessary to migrate between neighboring vent sites along the EPR.

Despite limited swimming capabilities during most or all of their planktonic life, larvae may affect their dispersal through behaviors that alter their position above the seafloor. Larvae of species living in shallow water exhibit a variety of behaviors that result in stratification of their populations in the water column (Forward, 1988; Sulkin, 1984; Young and Chia, 1987). Migrations of coastal larvae may occur daily in response to light, tidally in response to salinity or temperature, or ontogenetically (i.e., over the life span of the larva). Ontogenetic migrations typically involve upward floating or swimming during early larval stages (when lipid reserves are replete), maintenance of position during

* Corresponding author. Tel.: +1 508 289 2683; fax: +1 508 457 2194.
E-mail addresses: dmcgillicuddy@whoi.edu (D.J. McGillicuddy Jr.), j.william.lavelle@noaa.gov (J.W. Lavelle), ant@ldeo.columbia.edu (A.M. Thurnherr), lmullineaux@whoi.edu (L.S. Mullineaux).

0967-0637/$ - see front matter © 2010 Elsevier Ltd. All rights reserved.
doi:10.1016/j.dsr.2010.04.003

mid-stages, and sinking or downward swimming at late stages, when the larva has depleted lipids (and possibly grown a shell) and is ready to settle. This sort of ontogenetic migration appears to enhance retention of larvae in estuarine environments, as different life stages exploit opposing flows in these two-layer systems to minimize net transport from their source region (Dittel and Epifanio, 1990; Thiebaut et al., 1992). In deep water, we do not expect larvae to migrate in response to light, temperature, or salinity cues, but we do expect that ontogenetic migrations are possible, given their general prevalence in invertebrate larvae. In this study, we consider two different strategies likely to be exhibited by larvae in deep water: (1) 'passive' (directional swimming and/or buoyancy are either weak or compensating, so the larvae are passive tracers within the flow), and (2) 'balloonist' (upward movement shortly after fertilization and downward movement shortly before settlement). Balloonist larvae may achieve ontogenetic change in vertical position behaviorally, or through changes in buoyancy during larval development. Upward transport of larvae can also be brought about via their entrainment in buoyant plumes of vent fluid (Kim et al., 1994).

Our objective herein is to investigate the processes regulating larval dispersal along the EPR. We track a large number of particles subject to fluctuating circulation over an axially symmetric ridge and examine the sensitivity of larval transport and retention to several life history parameters, including larval behavior (passive versus balloonist) and length of the precompetency period. An ensemble of simulations spanning a seven-month period of measured currents provides the basis for generating statistics on the time-mean and fluctuating aspects of larval dispersal.

We note that our idealized two-dimensional model does not represent along-axis variations in hydrodynamic and ecological characteristics of this environment. However, several aspects of the EPR lend themselves to two-dimensional approximation. To begin with, ridge topography is to first order symmetric in the across-ridge direction, and roughly homogeneous in the along-ridge direction over distances on the order of 100 km. Moreover, analysis of current meter data along the ridge at 9°10′, 9°30′, and 9°50′N suggests coherence of velocity in the along-ridge direction (Thurnherr et al., submitted). Although the present model is far from complete, we view these simulations as a first step toward implementation of spatially explicit coupled physical–biological models of larval transport in this complex regime, expanding upon earlier models of larval transport that assumed spatially homogeneous currents (Marsh et al., 2001).

2. Methods

Circulation over an idealized 2D ridge was based on a primitive equation, baroclinic, hydrostatic, f-plane (latitude=9.833°N) model described in Lavelle (2006). The model consists of equations for horizontal and vertical velocities, pressure, potential temperature, salinity, density, and turbulent viscosities and diffusivities in both horizontal and vertical directions. Explicit mixing for momentum and other properties was parameterized according to Smagorinsky (1993). Outward propagating baroclinic waves were absorbed at the domain's edge using sponge layers (Lavelle and Thacker, 2008). Invariance of all equations in the along-ridge direction was assumed.

Model equations were discretized using finite volume expressions on a rectangular, z-level C-grid (256×128 cells), stretched in ridge-orthogonal (x), and vertical (z) directions. The highest grid resolution (Δx=440 m, Δz=12.5 m) was located at the ridge crest, coarsening to Δx=2.5 km, and Δz=50 m in the far-field. The solution domain extended upward to the rigid-lid sea surface and to a distance of 150 km at both sides of the ridge. Boundary conditions were cyclic in the x-direction and mixed (zero or zero-gradient) in the z-direction. At each time step, discretized equations for momentum and continuity were consolidated into a Helmholtz equation for pressure that was solved using multigrid methods. Momentum equations were leap-frogged in time, with an Asselin filter applied at each time step. Heat and salt equations utilized upstream differencing, suppressing numerical diffusion using the algorithm of Smolarkiewicz and Margolin (1998).

Bathymetry (H) was represented by an axially symmetric analytic function

$$H = H_{deep} - H_{relief} e^{-(|x-x_0|/\sigma)},$$

where x is distance in the east–west direction, x_0 is the location of the ridge crest, H_{deep}=3200 m, H_{relief}=700 m, and the e-folding distance σ is 6 km. These parameters were estimated by fitting ridge-normal transects of bathymetric data of the 9–10° segment of the EPR described in Wilcock et al. (1993). This z-level model represents bathymetry in 'stair-step' form; the computational artefact resulting from this discretization was reduced by utilizing the highest spatial resolution (128 vertical cells) practical considering the total time (4782 h) and time step (90 s) of the calculation. Background potential temperature and salinity profiles were taken from the World Ocean Atlas (Conkright et al., 2002), with smoothing applied to property gradients in the upper 250 m.

Our approach is to force the model with a time series of far-field currents, allowing the model interior to adjust dynamically to that forcing. No data are available to provide such forcing directly, so we must rely on inference from existing current measurements near the ridge. Details of this primitive inverse calculation are provided in Appendix A.

Currents for the inverse calculation were measured at a depth of 175 m above the bottom at the axis of the EPR at 9°50.9′N, and 104°17.6′W during the period May 2 through November 20, 1999. The observations were made with an Aanderaa RCM7 current meter encased in an RCM8 pressure housing for deep ocean use. Basic quality control was carried out by examining the data for anomalous values, but none were found, so the entire record was retained. A total of 4872 of these hourly sampled velocity measurements were used to construct the forcing time series. Forcing thus contained frequency components ranging from 0.5 h^{-1} to 0.205×10^{-3} h^{-1}. Model currents were spun-up from rest over the ten-day period prior to May 2, 1999, with the forcing ramped up to full amplitude during the first five days.

As formulated, the model does not explicitly represent the hydrodynamic effects of the fluid emanating from hydrothermal vents. Motion caused by the buoyancy of vent discharge, or even of vent field discharges, will affect regional flow only in a minor way and only locally at horizontal scales that are too small to be resolved by a regional-scale model grid (Lavelle, 1997). Thomson et al. (2003) reported buoyancy-driven convergent horizontal flows of several cm s^{-1} in the deep axial valley of the Endeavour segment of the Juan de Fuca Ridge. Flow of similar origin is not likely to be significant at the EPR, however, because the axial summit trough, where it exists on the EPR, is only a few meters deep (Fornari et al., 1998). Of course, plume dynamics play a primary role in small-scale flows that can retain larvae at their vent of origin (Bailly-Bechet et al., 2008), but our purpose here is to examine the fate of larvae that escape such localized flows and become subject to ambient currents.

Lagrangian transport of the numerical larvae was estimated from the hydrodynamic simulations using ensembles of particles released in the flow. Three-dimensional trajectories were

computed from the modeled velocities, assuming homogeneity of the velocity field in the along-axis direction. See Werner et al. (1993) and Blanton (1995) for more details on the particle tracking algorithm used in this study. In short, time series of three-dimensional position vectors are computed from modeled velocities using fourth-order Runge–Kutta integration with adaptive stepsize control (Press et al., 1986).

In order to bracket a realistic range of larval behaviors, particles were released at 10, 75, 125, 175, and 225 m above bottom (mab) at the ridge crest. The 10 mab releases are intended to mimic passive larvae, whereas the releases at 75 mab and greater reflect a balloonist strategy whereby larvae rise into the water column by swimming, buoyancy, or via convection in vent plumes (not explicitly resolved by the model). In either case, the rise time is sufficiently short (hours to days) so that horizontal transport during the transit upward constitutes only a small fraction of the total transport during the larval phase.

Similarly, the vertical movement during settlement is not explicitly represented. At any time the numerical larvae pass over the ridge crest after their precompetency period, and they are assumed to settle at the bottom instantaneously. Clearly, this approach could overestimate settlement insofar as horizontal currents are swift enough to sweep larvae off-axis during the finite time it takes them to descend. However, given the uncertainties in settlement cues and behavioral responses to those cues, we leave the detailed dynamics of the settlement process to future studies.

This model does not include the processes by which larvae are recruited into local populations. Moreover, we assume that the ridge crest is uniformly a suitable habitat for newly settled larvae. This is clearly not the case in the real ocean, as the organisms of interest require hydrothermal vent environments to survive as adults. Population connectivity between discrete vent communities will be the subject of future work with a fully three-dimensional model. The idealized simulations presented herein constitute a first step in exploring the basic patterns of larval transport and dispersion in this complex environment.

The larval life span specified for these experiments is thirty days, similar to that measured for the vent tubeworm *R. pachyptila* larvae in its non-feeding stage, and representative of larval life span in a variety of invertebrate species. Although larval life spans of several months or longer are possible (Scheltema, 1971), horizontal transport during such extended larval periods would carry larvae well beyond the ridge segment for which the currents simulated herein are representative. The impact of precompetency periods ranging from 5 to 25 days is examined via sensitivity analysis. We recognize that mortality can be significant on these time scales, yet we neglect these effects in order to focus our analysis on the physical–biological interactions that control larval transport in this regime.

3. Results

3.1. Simulated currents

Using forcing inferred from the current meter data (Appendix A), the model provides a realistic simulation of the observed ridge crest currents (Fig. 1). Cross-ridge (zonal) flows are on the order of 10 cm s^{-1}, and subtidal along-ridge (meridional) flows are 4–8 cm s^{-1}. Velocity fluctuations are an order of magnitude larger than the mean flows (Table 1), the latter of which contain only 0.9% of the total kinetic energy. Longer-period oscillations are more prominent in the meridional direction than in the zonal direction. Simulated velocities are highly correlated with observations, and the model captures the standard deviations of the observed currents to within 5–7%. Root-mean-square differences between simulated and observed velocities are 50% or less of the standard deviation.

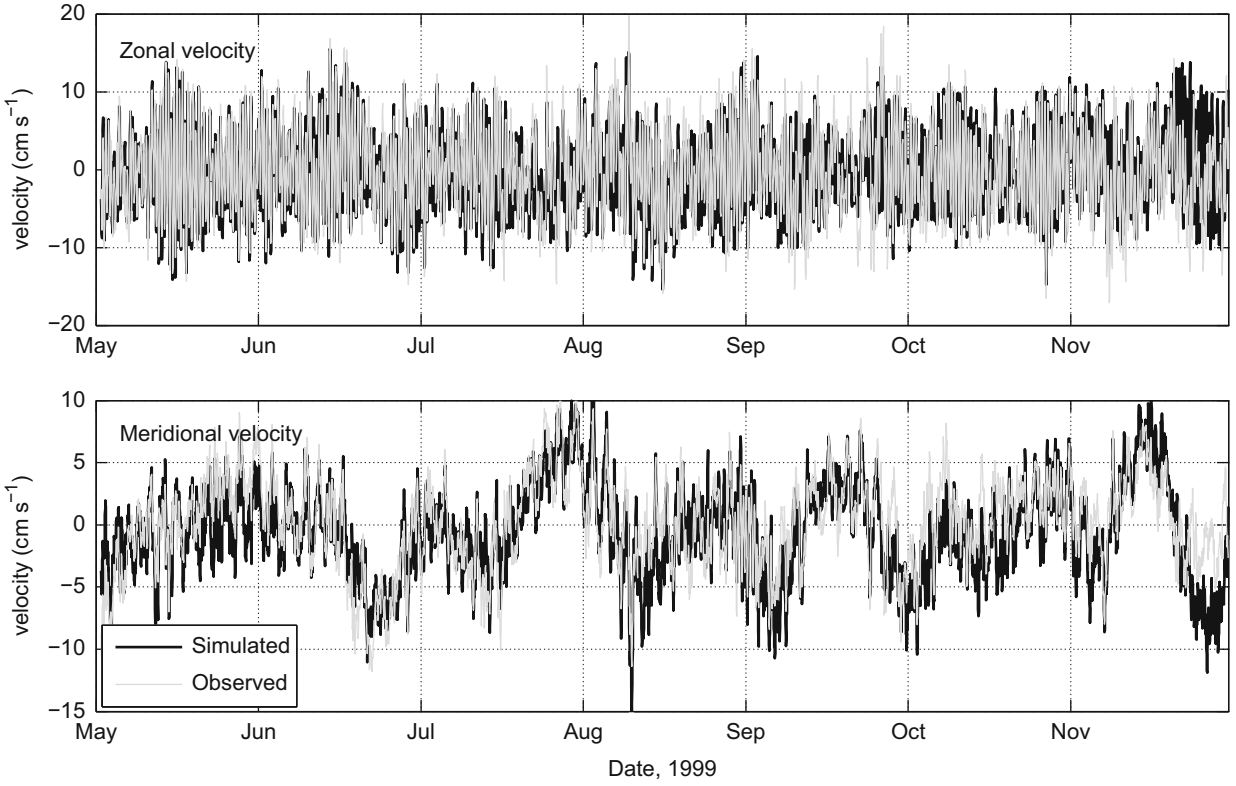

Fig. 1. Simulated and observed currents 175 mab on the EPR ridge crest at 9°50′N during May–November 1999: (top) zonal (east–west) velocity; and (bottom) meridional (north–south) velocity.

Table 1
Comparison of observed and modeled zonal (u) and meridional (v) velocities (cm s^{-1}), May–November, 1999. Total number of observations used in the comparison is 4872.

	Observed		Modeled	
	u	v	u	v
Mean	−0.29	−0.55	−0.22	0.13
Standard deviation	5.48	3.92	5.8	3.7
RMS difference	u: 2.14 v: 1.97			
Correlation	u: 0.85 v: 0.80			

Currents in the vicinity of the ridge contain significant across-ridge and vertical structure in both their time-mean and fluctuating components (Figs. 2 and 3). Strongest currents occur along the flanks of the ridge, with a time-mean of ca. 5 cm s^{-1} directed poleward on the western flank and equatorward on the eastern flank (Fig. 2B). These meridional jets span ca. 600 m in the vertical, from 2400 to 3000 m depth, and extend ca. 10 km in the zonal direction. Transport in the two jets averages 0.19 and −0.34 Sv over the course of the seven month simulation. The simulated jets are associated with significant perturbations to the density field (Fig. 2), owing to the fact they are in approximate geostrophic balance. Specifically, isopycnals tend to dome upward

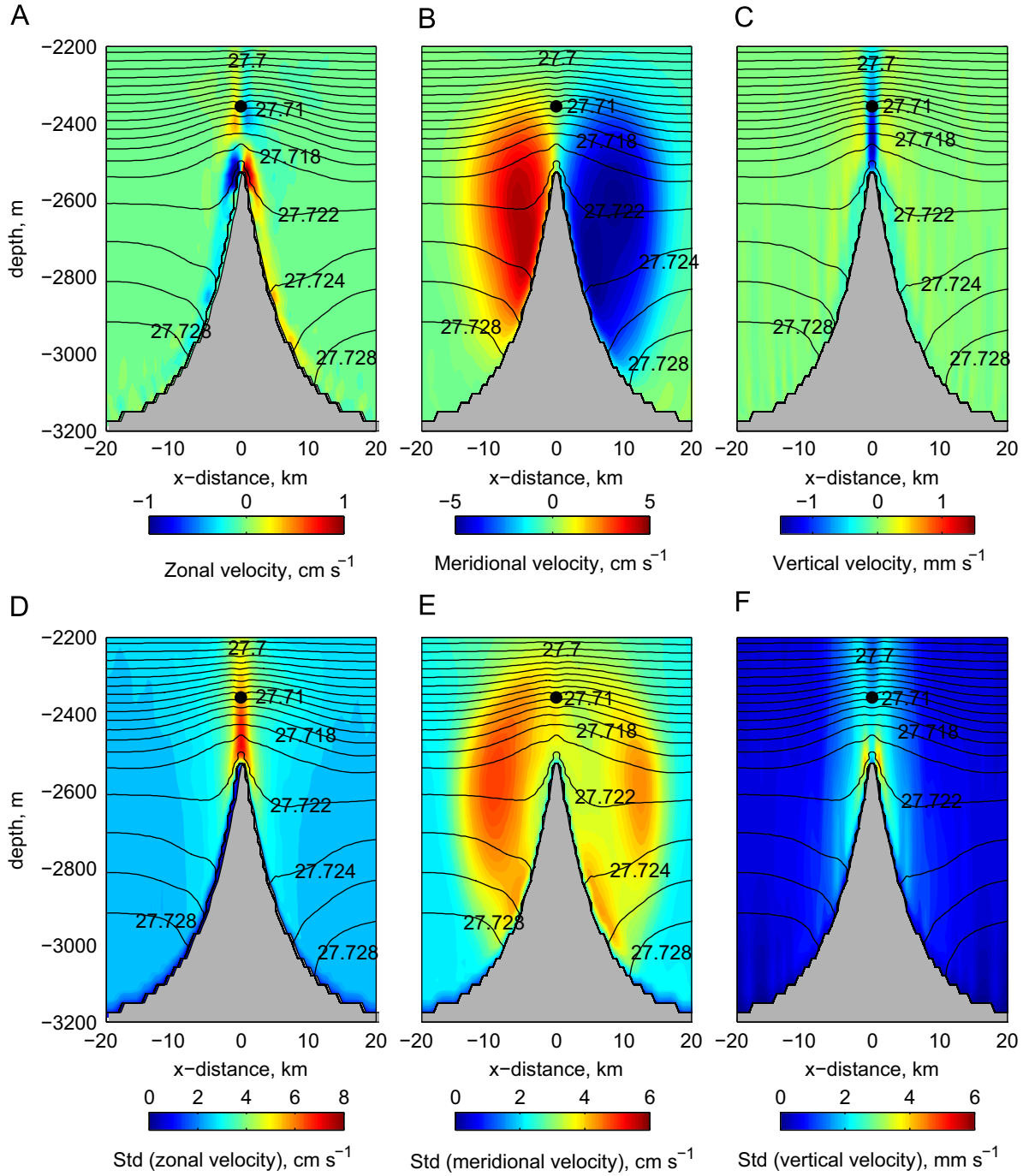

Fig. 2. Means and standard deviations of velocities in the zonal (A,D), meridional (B,E), and vertical (C,F) directions simulated for the period May–November, 1999. The black dot indicates the location of the current meter record comparison shown in Fig. 1. Time-mean potential density contours for the same time period are superimposed on each panel.

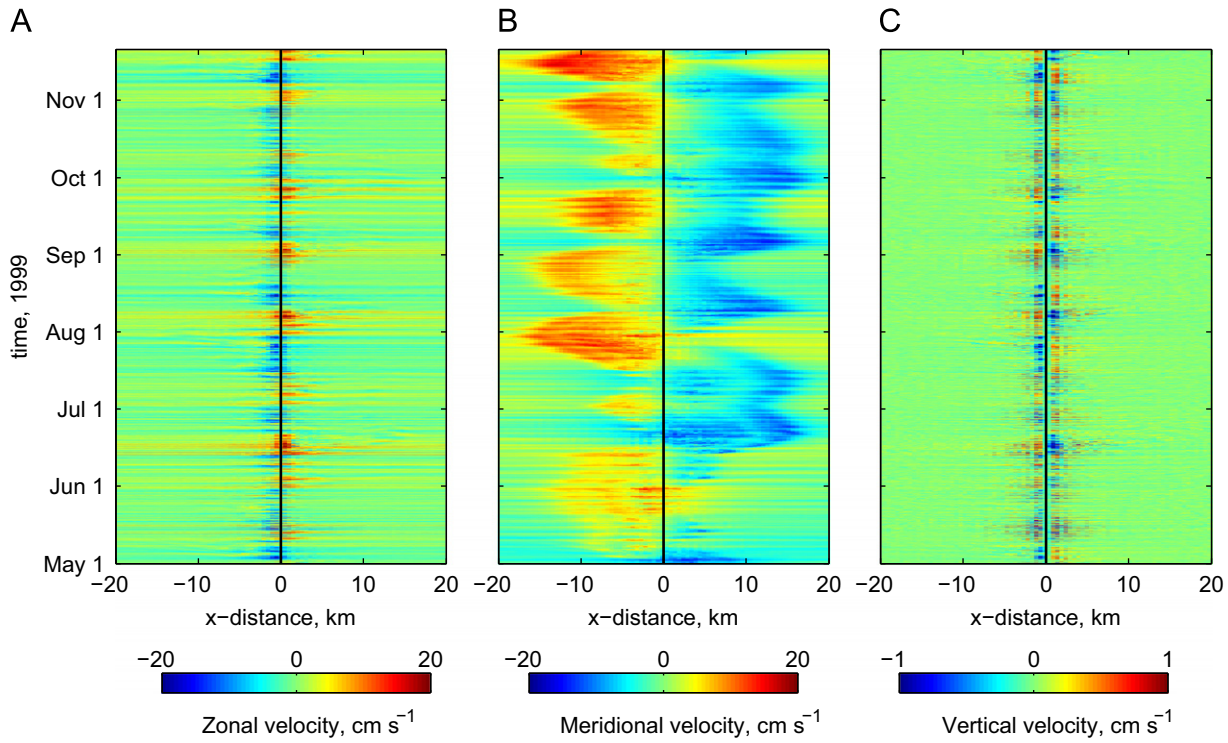

Fig. 3. Time series of simulated currents within ±20 km of the ridge axis at 2500 m (depth of the ridge crest) in the zonal (A), meridional (B), and vertical (C) directions.

above the ridge and plunge downward along the flanks of the ridge. A time-averaged high-resolution hydrographic cross-section at the EPR 9°N site is qualitatively consistent with these isopycnal deflections (Thurnherr et al., submitted).

Extensive validation of the simulated jets is not possible due to a paucity of direct measurements of these currents. Nonetheless, available observations are generally consistent with the model results. For example, a time-mean velocity profile derived from a moored profiler located 10 km west of the ridge axis at 9°30′N confirms the existence of the flank flow predicted by the model (Fig. 4). Although the magnitude of the observed current falls within the envelope of simulated mean profiles between the crest and 15 km off-axis, the vertical extent of velocity maximum is broader in the model than in the observations. The fact that the velocity profile observations come from a time period different from the current meter record used to force the model suggests the flank currents are a persistent feature of the mean circulation of the ridge system. This result was confirmed by performing an additional hydrodynamic simulation in which the model forcing was derived from a velocity record 128 mab at the ridge crest contemporaneous with the off-axis current meter presented in Fig. 4. Long-term mean flows and their variability were very similar to those presented in Figs. 1–4.

Additional evidence for northward flow west of the ridge comes from a tracer release experiment at the EPR 9–10° ridge segment in November–December 2006 (Jackson et al., 2010). Direct inference of the flow speed is not possible because the time interval over which the tracer resided in the jet (as opposed to ambient waters) is not known. A small part of the tracer moved from 9°30′ to 9°50′ in 33 days, suggesting a minimum meridional velocity along the flank of 1–2 cm s^{-1} (Jim Ledwell, personal communication).

A transect of velocity observations from a lowered acoustic Doppler current profiler (LADCP) during the same study detected residual flows northward to the west of the ridge and southward to the east of the ridge, as in the model result (Thurnherr et al., submitted). Similarly sheared mean flow is present in other regimes, such as the Juan de Fuca Ridge at 45°N (Cannon and Pashinski, 1997), suggesting this phenomenon may be a common characteristic of mid-ocean ridge systems. Essential to the formation of these topographically trapped flows are the Earth's local vertical rotation rate and advective nonlinearities. Details of the flow patterns depend on the topography of the ridge, local stratification, and the ambient currents.

Long-term mean flows in the zonal and vertical directions are weaker and confined to the region close to and above the crest (Fig. 2A,C). However, shorter-term zonal mean flows over the EPR are not as weak as those depicted here; monthly mean zonal flows calculated from the current meter data vary between −1.2 and +1.2 cm s^{-1}. What this serendipitously low seven-month mean flow period reveals is a weak recirculation cell above the ridge crest. Divergence of the zonal flow at crest depth and convergence several hundred meters above leads to downward vertical flow in a thin column above the crest and a broader upward flow in the adjacent waters. This pattern is reminiscent of the circulation that maintains the so-called "cold dome" above seamounts (Brink, 1995; Lavelle, 2006). Unfortunately there are no reliable measurements of vertical velocity above the ridge crest, so the realism of the simulated downwelling cell cannot be assessed directly.

In contrast to the ridge crest, where standard deviations in velocity are much larger than the mean, standard deviations of the ridge flank currents are approximately the same magnitude as the mean flows (Fig. 2). Further insight into the nature of this variability is provided by time series of velocity components across the ridge at the depth of the crest (Fig. 3). The location and spatial extent of the ridge flank jets fluctuate in time, with their far edges sometimes extending to nearly 20 km off-axis (Fig. 3B). Poleward and equatorward transports are generally not balanced. On a few occasions, subtidal meridional flow on both sides of the ridge has the same direction. However, most of the time the two jets flow in opposite directions, with the interface between them

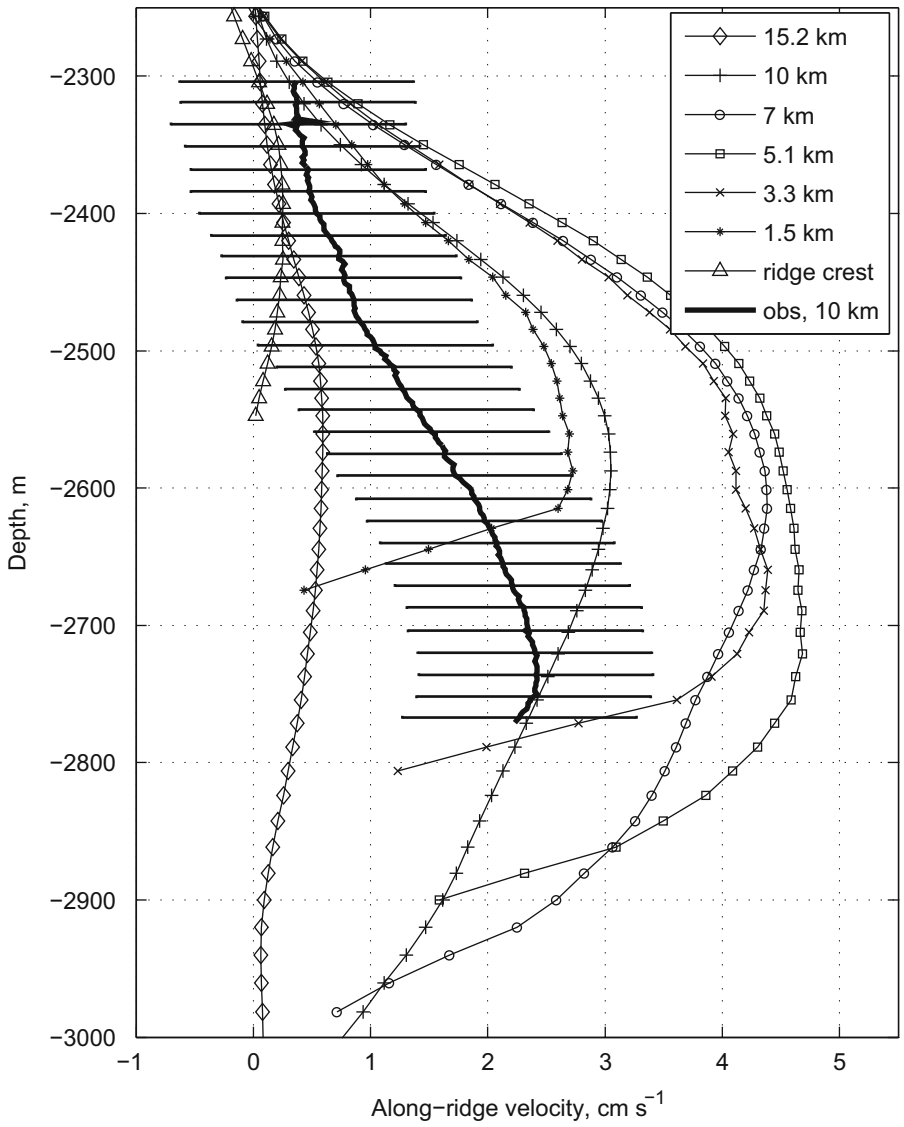

Fig. 4. Comparison of vertical profiles of time-mean along-ridge velocity simulated at several cross-axis locations in the model with observations from a moored profiler located 10 km west of the EPR ridge crest at 9°30′N. The latter profile consists of means and standard errors for the entire deployment November 2006–November 2007; standard errors are plotted every eighth data point. Note that variations in vertical extent of the simulated profiles reflect the underlying model bathymetry.

moving back and forth across the ridge crest ($x=0$). Cross-ridge displacement of the interface is also expressed in the zonal and vertical velocity components (Fig. 3A,C): eastward flow coincides with upwelling on the western flank and downwelling on the eastern flank, whereas westward flow coincides with downwelling on the western flank and upwelling on the eastern flank. An important consequence of this back-and-forth sweeping of the ridge current system is that velocities at the ridge crest are periodically impacted by both jets, enhancing the subtidal frequency components of the flow in the meridional direction relative to those in the zonal flow—a characteristic clearly evident in the current meter record (Fig. 1).

3.2. Lagrangian visualization of the flow patterns

To illustrate some key characteristics of the transport patterns, passive particles were released instantaneously along a cross-ridge transect and tracked during an example one-month time period (Fig. 5). Particle displacements are relatively modest amongst those released at 225 m above the depth of the ridge crest, with lagrangian trajectories spanning approximately 100 m in the vertical and 40 km in the along-ridge direction. Vertical and along-ridge displacements increase dramatically with depth, such that trajectories of the particles released at 10 m above the depth of the ridge crest span 500 m in the vertical and 150 km in the along-ridge direction. Particles released above the flanks of the ridge are particularly prone to large displacements as they become entrained into current jets along the ridge (Figs. 2 and 3). Episodic reversals in the cross-ridge flow can transport particles from one side of the ridge up and over the crest and back down the other side of the ridge. This tendency is best visualized in animated presentations of these results, available in the "cross_section_release" subdirectory of the supplemental documentation.[1]

Because these trajectories are derived from an example one-month time period of simulation, they do not precisely mimic the mean properties of the flow depicted in Fig. 2. Nevertheless, some

[1] Also available at http://science.whoi.edu/users/mcgillic/papers/epr2d/movies/cross_section_release/.

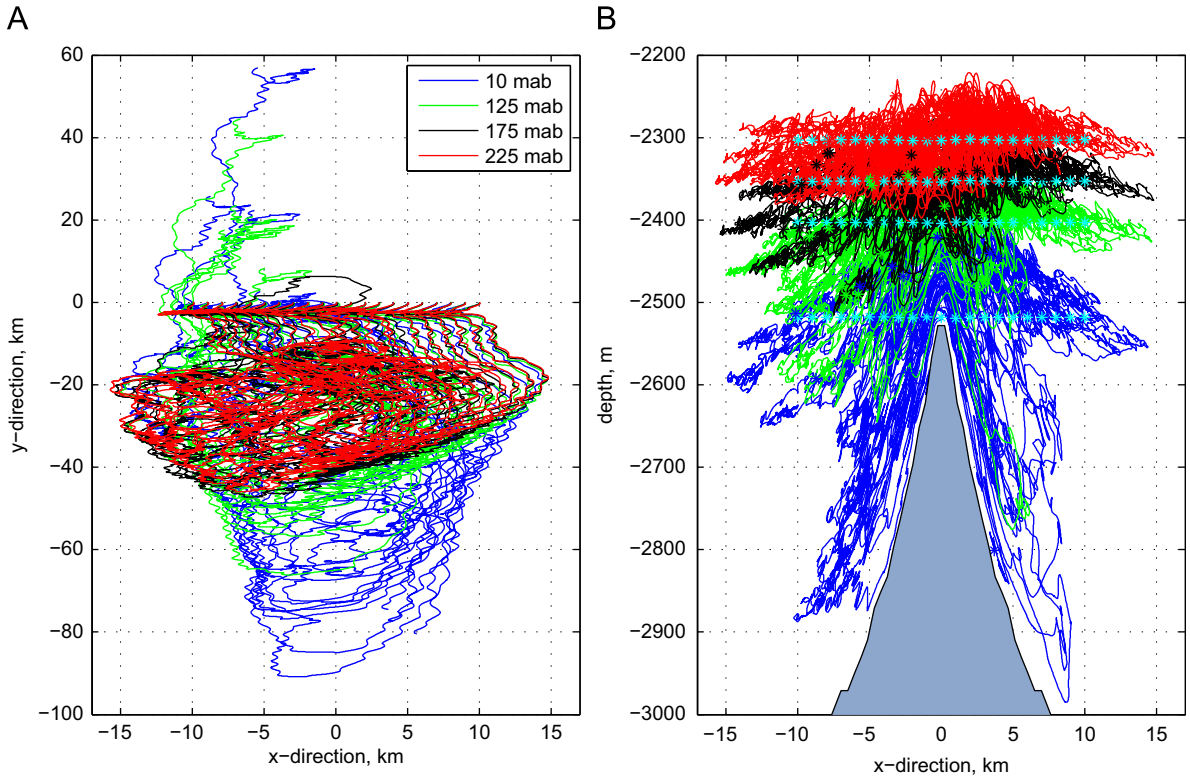

Fig. 5. Simulated particle trajectories for a one-month period from September 1, 1999 to October 1, 1999 presented in plan view (A) and vertical cross-section (B). Four sets of particles were released simultaneously at heights of 10 (blue), 125 (green), 175 (black), and 225 m (red) above the depth of the ridge crest. Horizontal spacing of the release points was 1km, spanning 20 km in the cross-ridge direction. Release locations are indicated by light-blue dots.

aspects of the mean flows are evident, such as the tendency for particles in the ridge flank currents to be transported poleward on the west flank of the ridge and equatorward on the east flank (most visible in particles released 10 and 125 mab). Further aloft, the flow during this time period is predominantly southward, a result that is also apparent in trajectories of particles released continuously at the ridge crest (Fig. 6; see Section 3.3 below).

3.3. *Dispersal of simulated larvae with a 30-day life span*

Larval dispersal patterns were simulated by releasing particles at the ridge crest every 12 min at depths of 10, 75, 125, 175, and 225 mab in the flow simulated from May to November 1999. Each particle was tracked for a larval life span of 30 days. Animated presentations of particle trajectories for September–October are available in the "time_dependent_release" subdirectory of the supplemental documentation.[2] With this large ensemble of particles (total 108,000) for the period May to November, it is possible to compute probability density functions (pdfs) of larval dispersal patterns as a function of time and space (Fig. 6). Monthly distributions of trajectory endpoints indicate that the numerical larvae can travel up to hundreds of km in the along-axis direction, but their net displacement in the cross-axis direction does not exceed ± 20 km during their thirty-day life span. Patterns of dispersal vary significantly in time. In June–July and August–September cases, maximum dispersal distances were up to 200 km to the south of the release point (a distance that exceeds the total length of the 9–10°N ridge segment). In June–July, almost 50% of the total number of particles exceeded 100 km displacement, with a bimodal distribution (one to the NNW and the other to the SSE). Dispersion is also highly sensitive to vertical positioning. Particles farther off the bottom traveled shorter distances and had a higher probability of resupply to the ridge crest.

Overall settlement rates of the simulated larvae, calculated as the fraction of particles in the water column directly above the ridge crest at the end of the 30-day larval life span, ranges from $<1\%$ to nearly 5% (Fig. 7). As stated in the Methods section, these estimates assume instantaneous movement of the larvae from the water column to the bottom, neglecting potentially important details of the settlement process. For example, a balloonist larva overlying the ridge crest at the end of its larval life span could be swept away from suitable habitat in the finite time required to reach the bottom. Similarly, a larva just off-axis could be transported toward favorable habitat during descent. Explicit modeling of the settlement process, including behavioral response to environmental cues, is an important avenue for future research.

Simulated settlement systematically increases with height off the bottom of the initial release points, such that particles released 225 mab are approximately three times more likely to be located over the ridge crest at the end of the larval life span (Fig. 7). Temporal variations in settlement are substantial, with more than fivefold differences amongst the bi-monthly bins. These variations reflect time-dependence in dispersal, which fluctuates with the hydrodynamic regime during each bi-monthly period (Fig. 6). For example, the dramatic decline in settlement in June–July resulted from shearing of the larval distributions into two distinct peaks located at NNW and SSE of the ridge crest, such that a very small proportion of

[2] Also available at http://science.whoi.edu/users/mcgillic/papers/epr2d/movies/time_dependent_release/.

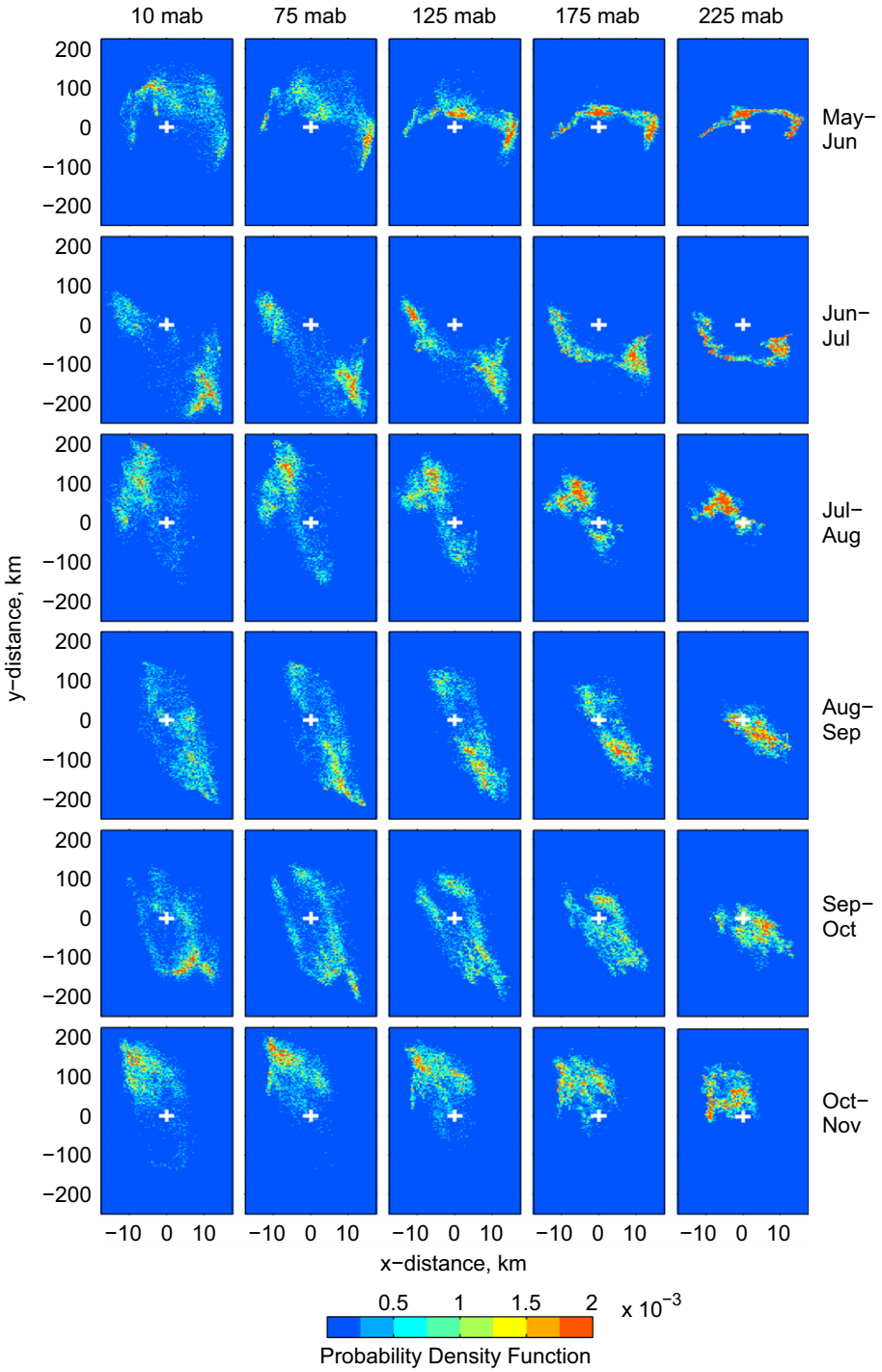

Fig. 6. Dispersal of particles released every 12 min from May to October 1999 at 10, 75, 125, 175, and 225 mab on the ridge crest (release location indicated by white cross). Final positions of each particle at the end of the 30-day larval life span were binned into control volumes with dimensions of 0.44 and 2.5 km in the cross- and along-ridge directions, respectively. Probability density functions were computed for each of the five depths during six bi-monthly periods: May–June, June–July, July–August, August–September, September–October, and October–November. Particles were released during the first month of each bi-monthly period. The bi-monthly periods overlap in time because the particles released at the end of the first month do not reach the end of the larval life span until the end of the second month. Color shading represents the number of particles residing in each bin, normalized by the total number of particles in each bi-monthly period (3600).

the larvae resided above favorable habitat at the end of the larval period.

Despite these dramatic temporal variations, it is still meaningful to compute time-mean pdfs of larval dispersal for the seven month simulation (Fig. 8, top row). The northwest-to-southeast orientation of the pdfs results from the tendency for mean flow to the north on the western flank of the ridge, and southward flow on the eastern flank of the ridge (Fig. 2B). Decrease in dispersal distance with height above bottom reflects less vigorous currents aloft.

3.4. *Influence of precompetency and cued settlement on dispersal*

The preceding results are based on an assumption that precompetency period is the same as the larval life span. If the

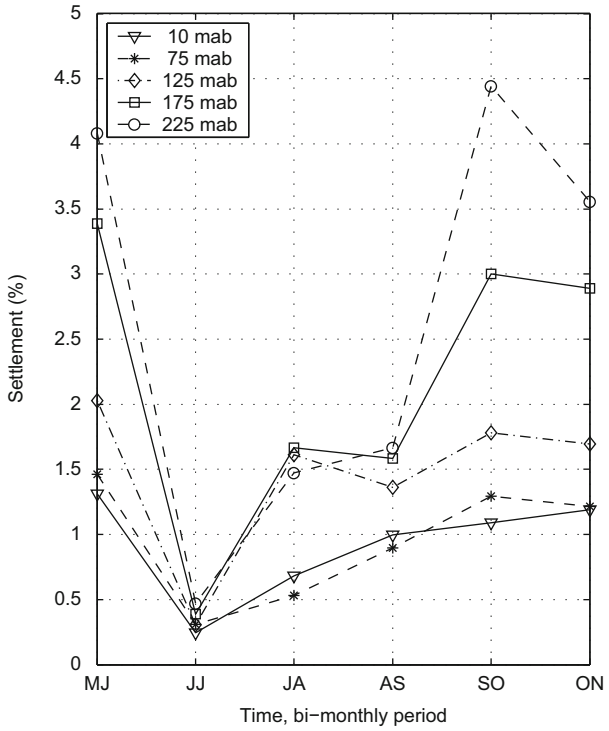

Fig. 7. Time series of settlement of numerical larvae, calculated as the fraction of particles with horizontal positions overlying the ridge axis (bin width 0.44 km) at the end of the 30-day larval life span.

larvae have a precompetency period shorter than their life span, there is a longer time interval over which settlement can occur. If they have the ability to sense favorable habitat and settle on that cue, retention along the ridge can increase dramatically (Fig. 8, rows 2–4). Overall, the degree of retention is highly sensitive to the period of precompetency (Fig. 9). Even a modest decrease in precompetency period from the larval life span improves the odds of settlement by an order of magnitude or more: for particles released 10 mab, retention increases from less than 1% for a 30 day precompetency period (Fig. 7) to ca. 15% for a 25 day precompetency period (Fig. 9). This large increase in the proportion of larvae that settle successfully on the ridge reflects the fact that larvae with a precompetency period shorter than the life span benefit from a longer time interval over which settlement can occur (Jackson and Strathmann, 1981). Consequently, their exposure to suitable habitat is increased by the vigorous cross-ridge displacements induced by the time-varying flow (Figs. 1–3, 5). These cross-ridge displacements decrease with height off the bottom, and as such the increase in retention resulting from a decrease in the precompetency period is diminished, albeit still a factor of ten: for particles released 225 mab, retention increases from less than 3% for a 30 day precompetency period (Fig. 7) to ca. 30% for a 25 day precompetency period (Fig. 9). The trend of increasing retention with shortening precompetency is consistent throughout the range of parameter space examined herein, such that retention for a 5 day precompetency period varies from 50% (10 mab) to 75% (225 mab). For all depths, increase in the period of competency increases settlement along the ridge and decreases the number of larvae lost from the system (Figs. 8 and 9). Of course, these results are likely to depend on the assumptions that the simulated larvae have a perfect ability to sense suitable habitat below, and settle immediately on that cue. Again, more explicit representation of the settlement process would help shed light on these sensitivities.

4. Discussion

The complex system of currents simulated in this axially symmetric representation of the EPR influences planktonic larval dispersal in a number of ways. To begin with, along-ridge transport is sensitive to vertical position. During a thirty-day life span, passive larvae released 10 mab spanned ± 200 km in the along-ridge direction. In contrast, maximal transport distances for balloonist larvae released 225 mab were only about half that of their passive counterparts. Garcia Berdeal et al. (2005) noted a similar trend of decreasing dispersal with height above bottom in an analysis of ADCP current meter data from the Juan de Fuca Ridge, although those observations came from within an axial valley—a very different topographic setting from the EPR. The opposite trend (increase in dispersal with height above bottom) was inferred by Mullineaux et al. (2005) based on velocity profiles at the Juan de Fuca Ridge from Thomson et al. (1990) and Cannon and Pashinski (1997). Part of this discrepancy may be due to small-scale topographic effects on currents measured near the bottom at Juan de Fuca that are not resolved in our model. However, observations at the EPR between 9 and 10°N reveal currents directly over the crest tend to decrease with depth (Thurnherr et al., submitted), similar to the profiles used in the Mullineaux et al. (2005) analysis. Thus it seems that small-scale topographic effects are not the root of the apparent discrepancy. A more likely cause is the along-flank flow, which is more vigorous at crest depth than further up in the water column (Fig. 2B). Our inference that dispersal distances increase with depth, even though the horizontal velocities directly above the crest decrease with depth, is directly related to the presence of spatial variability in the velocity field. Such spatial variability is not accounted for in dispersal estimates derived from single current meter records.

Vertical position in the water column affects not only the transport distance but also the delivery of larvae to suitable habitat. Our simulations demonstrate that for the cases in which the precompetency period is the same as the larval life span, vertical position of the initial release points accounts for nearly threefold variations in time-mean settlement of larvae at the ridge crest. Whereas time-mean settlement was ca. 1% for particles released 10 mab, settlement of particles released 225 mab was almost 3% (Fig. 7).

Both dispersal and settlement vary significantly with time, owing to the fluctuating hydrodynamic environment characteristic of the EPR. Depending on flow conditions, net transport of larvae can occur in either direction along the ridge, with substantial variations in transport distance. Mean flows oriented to the north on the western flank of the ridge and to the south on the eastern flank of the ridge tend to orient larval distributions in the northwest–southeast directions, although the manifestations of such shear dispersion are highly time-dependent. Monthly mean settlement of larvae varies by an order of magnitude for the cases in which the precompetency period is the same as the larval life span.

Based on these results, it appears that the balloonist strategy of rising well above the ridge crest improves the odds for local retention of larvae, insofar as such behavior tends to isolate them from the vigorous near-bottom currents that are present along the ridge flanks. All other physical and biological factors being equal, species with a balloonist larval stage can presumably achieve a self-sustaining population with lower fecundity than those with a passive larval stage. In contrast, species with passive larvae would be better able to colonize a new area, by virtue of the longer dispersal distances associated with transport in strong near-bottom currents.

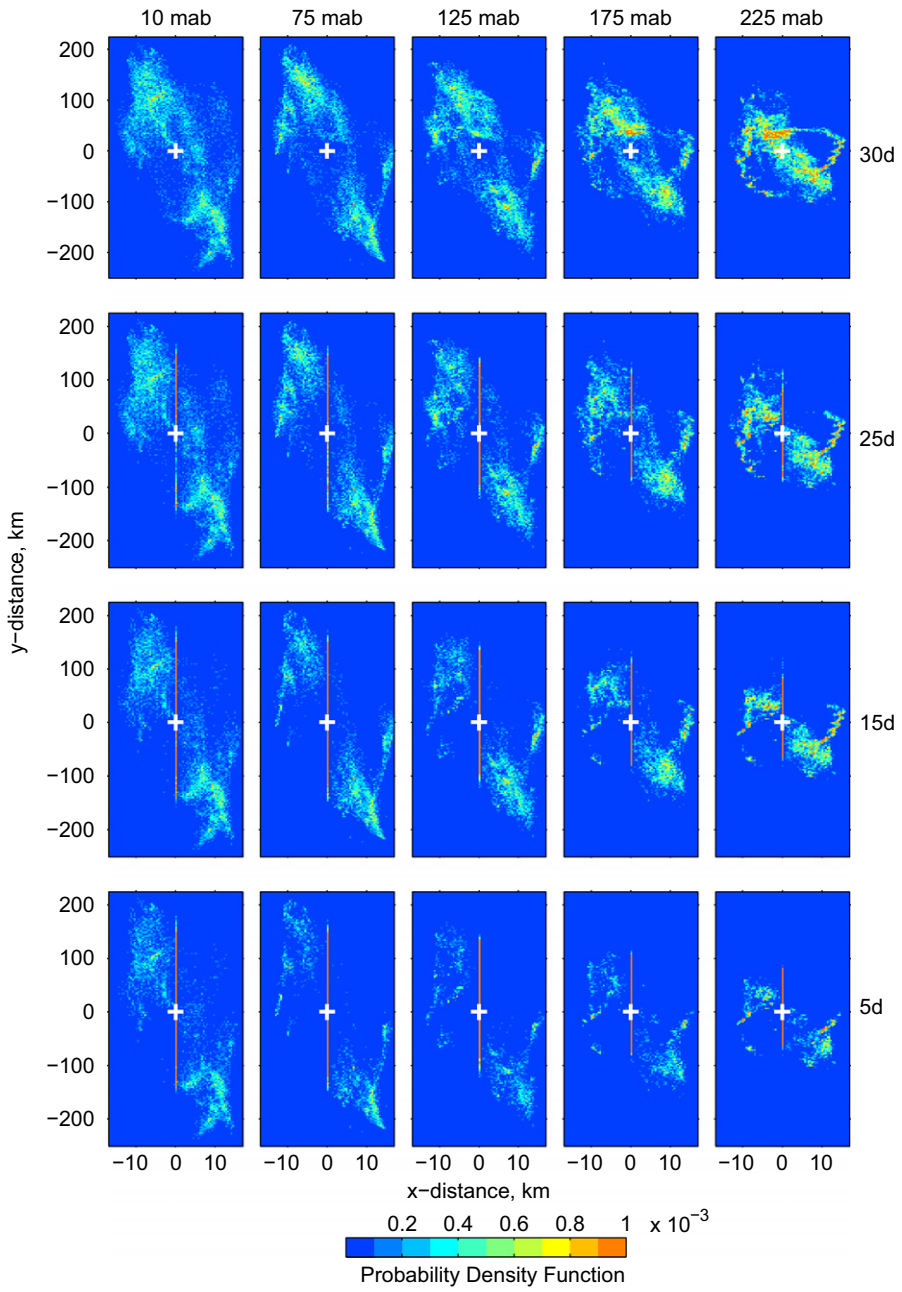

Fig. 8. Time-mean probability density functions for particles with various precompetency periods released every 12 min from May to October 1999 at 10, 75, 125, 175, and 225 mab at the ridge crest (release location indicated by white cross). Color shading represents the number of particles residing in 0.44×2.5 km^2 bins, normalized by the total number of particles released (108,000). Results for precompetency periods varying from 5 days up to the larval life span (30 days) are reported in different rows.

There is evidence for both long-distance colonization and local retention at the EPR. Mullineaux et al. (2010) describe drastic changes in species composition at the EPR subsequent to a catastrophic eruption during which all extant communities were destroyed. Of the new colonists detected after the eruption, one species had never been found on that ridge segment before, suggesting import of larvae from distant sources. On the other hand, Adams and Mullineaux (2008) detected correlations between larval supply and currents at the EPR that could be explained by local sources of larvae. Metaxas (2004) interpreted relative spatial homogeneity in planktonic larval abundance and flux at scales of 2 km and less at several vent sites in the northeast Pacific to suggest local retention. Local retention may also be facilitated by topographic confinement and circulation within deep rift valleys, such as is present at the Endeavour segment of the Juan de Fuca ridge (Thomson et al., 2003). However, given the strength of the currents observed in ridge systems, local retention would require a precompetency period of no longer than a day or two.

Our results are different from an earlier study (Marsh et al., 2001) of larval dispersal on the EPR 9–10°N ridge segment. Marsh et al.'s computations indicate that at the end of the 26 day life span, the along-axis distribution of surviving larvae peaked at the along-axis location of their release ($x=0$ in their Fig. 4c). More than 80% of the surviving larvae were located within ± 60 km of the release site, and the distribution was skewed to the south. The maximum along-axis dispersal distance was 103 km to the south. In contrast to the unimodal distribution predicted by Marsh et al., the along-axis distribution predicted herein is bimodal (Fig. 10). Only 50% of the larvae are located within 60 km of the release site,

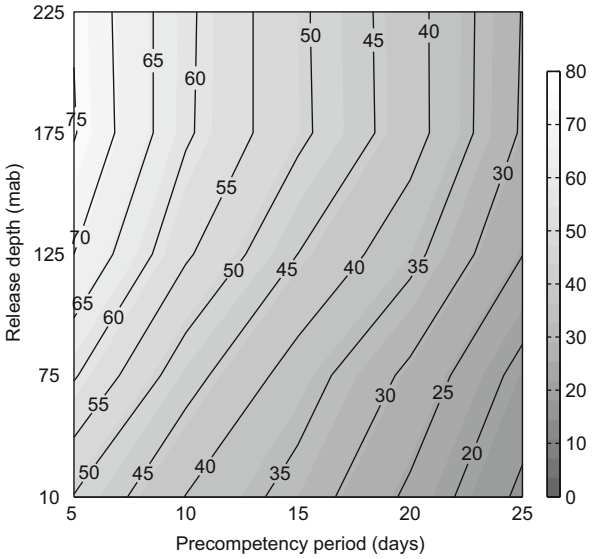

Fig. 9. Dependence of settlement on release depth and precompetency period. Settlement of numerical larvae occurs when their horizontal position is within a grid cell at the ridge crest (width 0.44 km) anytime after the precompetency period, but before the end of the larval life span. Shaded contours of settlement are expressed as a percentage of the total particles released.

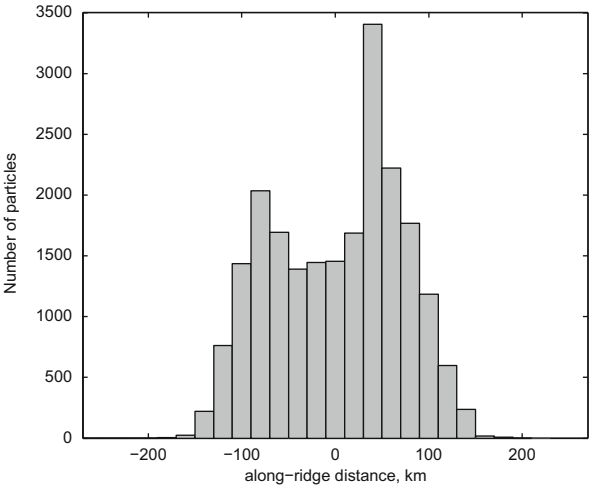

Fig. 10. Along-axis distribution of particles released every 12 min from May to October 1999 at 175 mab at the ridge crest. These are the same results as presented in the 175 mab panel of the top row of Fig. 7, plotted as a function of along-axis distance so as to be comparable with Fig. 4c of Marsh et al. (2001).

and peaks of the distribution reside at 50 km to the north and 100 km to the south of the release site. Locations of these peaks are near the maximum distances present in the Marsh et al. distribution, and the tails of the distribution predicted herein surpass their dispersal distances by fifty percent to the south, and a factor of three to the north.

Why are the results of the present study different from those of Marsh et al. (2001)? Although the two investigations were located at the same study site, our methods differ in both biological and physical aspects. First, the larval life span used herein (30 days) was slightly longer than that used by Marsh et al. to compute their along-axis distribution of survivors (26 days). Second, Marsh et al. assumed 100% mortality of larvae transported beyond 25 km of the ridge crest, whereas the present simulations did not include any mortality except that which occurs if a numerical larva is located off-axis at the end of its life span. Although Marsh et al. assumed all larvae within 25 km of the ridge crest to be "survivors," our settlement computations (Figs. 7 and 9) include only those larvae that are located directly above the ridge crest at the time of settlement. Thus the along-axis distribution of larvae presented in Fig. 10 reflects the pre-settlement condition (cf. 175 mab panel in the top row of Fig. 8) in order to be as comparable as possible to the Marsh et al. result.

Notwithstanding these differences in the biological assumptions used in estimating larval dispersal, the primary reason for the differences in the results of the two studies is the hydrodynamic basis of the transport computations. Whereas Marsh et al. used horizontal velocities observed at the ridge crest and assumed spatial uniformity in currents, the present study fits velocity observations with a hydrodynamic model to infer a dynamically consistent velocity field. Spatial structure in the velocity field (Figs. 2–5) underlies a key facet of our results, as the bimodal nature of the time-mean along-axis distribution (Figs. 8 and 10) is a direct consequence of mean southward flow on the eastern flank of the ridge and mean northward flow on the western flank of the ridge. Moreover, the presence of a vertical component to the motion of the larvae simulated herein provides them exposure to the more swift along-ridge flows during times when they are subject to cross-ridge displacement, resulting in greater along-axis transport overall.

It is important to note that the Marsh et al. (2001) study used a current meter record from a different time period (December 1999 to April 2000) than that used herein (May to November 1999). In comparing the two records, Marsh et al. found that the later time series yielded longer dispersal distances than the earlier record used in the present study. Therefore, were the comparison between these two approaches to be carried out using the same current meter record, the differences in dispersal would likely be even larger.

5. Conclusions

Although the physical model used herein is idealized, it provides a hydrodynamic environment that is significantly more complex than spatially uniform models used in some prior studies of larval transport in deep-ocean ridge systems. Energetic sheared flow along the ridge flanks significantly increases dispersion of passive larvae near the bottom, transporting them much farther and in more complex spatial patterns than a spatially uniform model based on ridge crest currents would predict. Of course, there remain a number of additional physical and biological complexities that must be grappled within future studies. To begin with, a fully three-dimensional model will be required to implement a realistic bathymetric setting that can accommodate along-axis variations in the hydrodynamic environment. Such models will also facilitate explicit representation of discrete vent communities, permitting detailed analysis of their interconnectivity from a larval perspective. Several biological aspects are also in need of additional study, including mortality during the larval stage, the specific behaviors by which newly spawned larvae ascend into the water column, as well as their responses to environmental cues for descent and subsequent settlement.

Models such as these could eventually be useful for predicting aspects of larval supply to, and colonization of, newly opened vents. In hydrodynamic systems similar to the EPR, when a new vent opens far from other active vents (e.g., $>$ 100 km) one might expect the initial colonists to be species that disperse predominantly in the strong, near-bottom currents. In contrast, initial colonists at a new vent opening in the neighborhood of other established vents (tens of km away) might be dominated by balloonist species. Near-bottom dispersers with very short precompetency periods also would be potential early colonists of neighboring new vents. At present, our understanding of vertical larval positioning behaviors in vent species is limited, but

vertical sampling in the field (expanding on efforts by Mullineaux et al. 2005 and others) should help us determine which species are dispersing at what heights above bottom. That information, in combination with inferences on precompetency period, should enable species-level predictions of initial colonists at new vents.

Acknowledgments

We gratefully acknowledge the support of NSF grant OCE-0424953, which funded the Larval Dispersion along the Deep East Pacific Rise (LADDER) project. JWL was supported by the National Oceanic and Atmospheric Administration's (NOAA) Vents Program and by NOAA's Pacific Marine Environmental Laboratory. Discussions with our LADDER colleague Jim Ledwell were very valuable to the analysis described herein. Comments and suggestions by three anonymous reviewers and Associate Editor Andrew Gooday were of great help in improving the original manuscript.

Appendix A. Inverse calculation for model forcing

A primitive inverse calculation is used to derive forcing that causes the model to mimic current meter observations above the ridge crest. Let the currents over the ridge over the time period $[0,T]$ at measurement interval dt be represented in rotary spectral form (e.g. Emery and Thomson, 1998) where temporal cyclicity of the currents is assumed

$$(u(t)+iv(t))^{measured}_{ridge} = A(\omega_n)e^{i\omega_n t}+A'(\omega_n)e^{-i\omega_n t} \quad 0<t<T \tag{A.1}$$

Here u and v are the north and east components of the current time series at time t, A, and A' are complex numbers, and $\omega_n = 2\pi n/T$ represents the set of frequencies where $n=\{0,1,2,\ldots,N/2\}$ and $N=T/dt$. In Eq. (A.1) and hereafter, a summation on the right hand side over all constituent frequencies is implied.

Analogous equations, but in slightly abbreviated form, can be written for the first model input time series at great distance from the ridge (A.2), the first model result at the ridge (A.3), and the second model input times series at great distance from the ridge (A.4)

$$(u+iv)^{model\ 1st}_{farfield} = Be^{i\omega t}+B'e^{-i\omega t} \tag{A.2}$$

$$(u+iv)^{model\ 1st}_{ridge} = Ce^{i\omega t}+C'e^{-i\omega t} \tag{A.3}$$

$$(u+iv)^{model\ 2nd}_{farfield} = De^{i\omega t}+D'e^{-i\omega t} \tag{A.4}$$

In practice, a reasonable choice for B and B' are the amplitudes A and A' of the currents measured at the ridge reduced by a factor of 0.5. An initial model run is made using forcing from Eq. (A.2). A comparison of the resulting model time series at the ridge (Eq. (A.3)) to the measured current time series at the ridge (Eq. A.1) is then used to make a better distant model current time series (Eq. (A.4)).

Suppose that the circulation model could be considered a transfer function and suppose that the transfer function were linear. Then the relationship of the time series at the ridge and in the distant ocean (Eqs. (A.2) and (A.3)) could be written

$$(u+iv)^{model\ 1st}_{ridge} = \int_0^T M(t-t')(u(t')+iv(t'))^{model\ 1st}_{farfield}\,dt' \tag{A.5}$$

where M represents the model transform function. Replacing the two current time series in Eq. (A.5) with their Fourier expansions (Eqs. (A.2) and (A.3)), we have

$$C(\omega_n)e^{i\omega_n t}+C'(\omega_n)e^{-i\omega_n t} = \int_0^T M(t-t')(B(\omega_n)e^{i\omega_n t'}+B'(\omega_n)e^{-i\omega_n t'})dt' \tag{A.6}$$

Similarly,

$$A(\omega_n)e^{i\omega_n t}+A'(\omega_n)e^{-i\omega_n t} = \int_0^T M(t-t')(D(\omega_n)e^{i\omega_n t'}+D'(\omega_n)e^{-i\omega_n t'})dt' \tag{A.7}$$

By the convolution theorem, Eqs. (A.6) and (A.7) yield

$$C(\omega_n) = M(\omega_n)B(\omega_n) \quad \text{and} \quad A(\omega_n) = M(\omega_n)D(\omega_n) \tag{A.8}$$

with like equations involving A', B', C', and D'.

Eliminating $M(\omega_n)$ from equation pair (A.8), as well as from the analogous primed variable equation pair gives

$$D(\omega_n) = \frac{B(\omega_n)A(\omega_n)}{C(\omega_n)} \quad \text{and} \quad D'(\omega_n) = \frac{B'(\omega_n)A'(\omega_n)}{C'(\omega_n)} \tag{A.9}$$

Eq. (A.4) can be re-expressed in the time domain with the Fourier coefficients from (A.9)

$$(u+iv)^{model\ 2nd}_{farfield} = \frac{BA}{C}e^{i\omega t}+\frac{B'A'}{C'}e^{-i\omega t} \quad 0<t<T \tag{A.10}$$

resulting in an improved estimate of the far-field forcing time series.

The circulation model is in fact not linear and the strong flank currents (Figs. 2–4) are partly supported by the nonlinearity of the governing equations. On the other hand, at high frequencies (including tidal frequencies), an assumption of dynamical linearity is often made. Thus, for a substantial part of the frequency spectrum of the measurements, Eq. (A.10) should provide a better estimate than Eq. (A.2) of the far-field forcing time series. Ultimately it is the correspondence of measured and modeled flow over the ridge crest summed over all frequencies (Fig. 1) that provides evidence of the utility of this primitive inverse approach.

In principle, there is no need to stop at the second estimate of the distant currents. However, a few pilot experiments we conducted suggested that the benefits of computing a third and fourth estimate were not worth the effort. Results presented herein use the second estimate of far-field currents to force the model. One additional practical matter in evaluating the coefficients of Eq. (A.9) must be mentioned. Very small values of C and C' at some ω_n lead to unrealistically large spectral coefficients for the second estimate, so that when $|A/C|>1$ or $|A'/C'|>1$, the ratio was reset to one. In other words, at each frequency the far-field amplitude must be less than or equal to the amplitude above the ridge.

The far-field u,v time series are used to determine a body force (F_B) or equivalently a horizontal pressure (P_0) gradient that drives the incident barotropic model flow. That force (or pressure gradient) is derived from simple balances that dominate the momentum equation at large distance from the ridge topography, i.e.

$$\frac{\partial u}{\partial t}-fv = -\frac{\partial P_0}{\partial x} = F_B^x \quad \text{and} \quad \frac{\partial v}{\partial t}+fu = -\frac{\partial P_0}{\partial y} = F_B^y$$

where u and v represent the far-field current time series first of Eq. (A.2) and then of Eq. (A.4).

Appendix B. Supporting Material

Supplementary data associated with this article can be found in the online version at doi:10.1016/j.dsr.2010.04.003.

References

Adams, D.K., Mullineaux, L.S., 2008. Supply of gastropod larvae to hydrothermal vents reflects transport from local larval sources. Limnology and Oceanography 53 (5), 1945–1955.

Bailly-Bechet, M., Kerszberg, M., Gaill, F., Pradillon, F., 2008. A modeling approach of the influence of local hydrodynamic conditions on larval dispersal at hydrothermal vents. Journal of Theoretical Biology 255, 320–331.

Berg, C.J., Van Dover, C.L., 1987. Benthopelagic macrozooplankton communities at and near deep-sea hydrothermal vents in the eastern Pacific Ocean and the Gulf of California. Deep-Sea Research 34, 379–401.

Blanton, B., 1995. DROG3D: user's manual for three-dimensional drogue tracking on a finite element grid with linear finite elements (see 〈http://www.opnml.unc.edu/Particle_Tracking/part_track.html〉), Program in Marine Sciences, University of North Carolina, Chapel Hill, NC.

Brink, K.H., 1995. Tidal and lower frequency currents above Fieberling-Guyot. Journal of Geophysical Research 100 (C6), 10,817–10,932.

Cannon, G.A., Pashinski, D.J., 1997. Variations in mean currents affecting hydrothermal plumes on the Juan de Fuca Ridge. Journal of Geophysical Research 102, 24,965–24,976.

Chevaldonné, P., Jollivet, D., Vangriesheim, A., Desbruyères, D., 1997. Hydrothermal-vent alvinellid polychaete dispersal in the eastern Pacific .1. Influence of vent site distribution, bottom currents, and biological patterns. Limnology and Oceanography 42, 67–80.

Conkright, M.E., Antonov, J.I., Baranova, O., Boyer, T.P., Garcia, H.E., Gelfeld, R., Johnson, D., Locarnini, A., Murphy, P.P., O'Brien, T.D., Smolyar, I. and Stephens, C., 2002. World Ocean Database 2001. NOAA Atlas NESDIS 42, 1: Natl. Oceanic and Atmos. Admin., Silver Spring, MD.

Dittel, A.I., Epifanio, C.E., 1990. Seasonal and tidal abundances of crab larvae in a tropical mangrove system, Gulf of Nicoya, Costa Rica. Marine Ecology Progress Series 65, 25–34.

Emery, W.J., Thomson, R.E., 1998. Data Analysis Methods in Physical Oceanography. Pergamon, New York 634pp.

Fornari, D., Haymon, R., Perfit, M., Gregg, T., Edwards, M., 1998. Axial summit trough of the East Pacific Rise 9°–10°N: Geological characteristics and evolution of the axial zone on fast spreading mid-ocean ridge. Journal of Geophysical Research 103 (B5), 9827–9855.

Forward, R.J., 1988. Diel vertical migration: Zooplankton photobiology and behaviour. Oceanography and Marine Biology: An Annual Review 26, 361–393.

Garcia Berdeal, I., Hautala, S.L., Thomas, L.N., Johnson, H.P., 2005. Vertical structure of time-dependent currents in a mid-ocean ridge axial valley. Deep-Sea Research I 53, 367–386.

Hoegh-Guldberg, O., Welborn, J.R., Manahan, D.T., 1991. Metabolic requirements of antarctic and temperate asteroid larvae. Antarctic Journal of the United States 26, 163–165.

Jackson, G.A., Strathmann, R.R., 1981. Larval mortality from offshore mixing as a link between precompetent and competent periods of development. American Naturalist 118, 16–26.

Jackson, P.R., Ledwell, J.R., Thurnherr, A.M., 2010. Dispersion of a Tracer on the East Pacific Rise (9°N to 10°N), Including the Influence of Hydrothermal Plumes. Deep-Sea Research I, 57, 37–52.

Kim, S.L., Mullineaux, L.S., Helfrich, K.R., 1994. Larval dispersal via entrainment into hydrothermal vent plumes. Journal of Geophysical Research 99 (C6), 12655–12665.

Lavelle, J.W., 1997. Buoyancy-driven plumes in rotating, stratified cross flows: Plume dependence on rotation, turbulent mixing, and cross-flow strength. Journal of Geophysical Research 102 3405–3418.

Lavelle, J.W., 2006. Flow, hydrography, turbulent mixing, and dissipation at Fieberling Guyot examined with a primitive equation model. Journal of Geophysical Research 111 (C07014), doi:10.1029/2005JC003224.

Lavelle, J.W., Thacker, W.C., 2008. A pretty good sponge: dealing with open boundaries in limited-area ocean models. Ocean Modelling 20 (3), 270–292.

Lutz, R.A., Jablonski, D., Rhoads, D.C., Turner, R.D., 1980. Larval dispersal of a deep-sea hydrothermal vent bivalve from the Galapagos Rift. Marine Biology 57, 127–133.

Marsh, A.G., Mullineaux, L.S., Young, C.M., Manahan, D.T., 2001. Larval dispersal potential of the tubeworm *Riftia pachyptila* at deep-sea hydrothermal vents. Nature 411, 77–80.

Metaxas, A., 2004. Spatial and temporal patterns in larval supply at hydrothermal vents in the northeast Pacific Ocean. Limnology and Oceanography 49 (6), 1949–1956.

Mullineaux, L.S., Adams, D.K., Mills, S.W., Beaulieu, S.E., 2010. Larvae from afar colonize deep-sea hydrothermal vents after a catastrophic eruption. Proceedings of the National Academy of Sciences, doi:10.1073/pnas.0913187107.

Mullineaux, L.S., Mills, S.W., Sweetman, A.K., Beaudreau, A.H., Metaxas, A., Hunt, H.L., 2005. Vertical, lateral, and temporal structure in larval distribution at hydrothermal vents. Marine Ecology Progress Series 293, 1–16.

Mullineaux, L.S., Speer, K.G., Thurnherr, A.M., Maltrud, M.E., Vangriesheim, A., 2002. Implications of cross-axis flow for larval dispersal along mid-ocean ridges. Cahiers de Biologie Marine 43, 281–284.

Mullineaux, L.S., Wiebe, P.H., Baker, E.T., 1995. Larvae of benthic invertebrates in hydrothermal vent plumes over Juan de Fuca Ridge. Marine Biology 122, 585–596.

Press, W.H., Flannery, B.P., Teukolsky, S.A., Vetterling, W.T., 1986. Numerical Recipes. Cambridge University Press, Cambridge.

Scheltema, R.S., 1971. The dispersal of larvae of shoalwater benthic invertebrate species over long distances by ocean currents. In: Crisp, D.J. (Ed.), Fourth European Marine Biology Symposium. Cambridge University Press, Cambridge, pp. 7–28.

Smagorinsky, J., 1993. Some historical remarks on the use of nonlinear viscosities. In: Galperin, B., Orszag, S.A. (Eds.), Large Eddy Simulation of Complex Engineering and Geophysical Flows.. Cambridge University Press, pp. 3–36.

Smolarkiewicz, P.K., Margolin, L.G., 1998. MPDATA: a finite-difference solver for geophysical flows. Journal of Computational Physics 140 (2), 459–480.

Strathmann, R.R., 1985. Feeding and nonfeeding larval development and life-history evolution in marine invertebrates. Annual Review of Ecology and Systematics 16, 339–361.

Sulkin, S.D., 1984. Behavioral basis of depth regulation in the larvae of *Brachyuran* crabs. Marine Ecology Progress Series 15, 181–205.

Thiebaut, E., Dauvin, J.-C., Lagadeuc, Y., 1992. Transport of *Owenia fusiformis* larvae (Annelida: Polychaeta) in the Bay of Seine. I. Vertical distribution in relation to water column stratification and ontogenetic vertical migration. Marine Ecology Progress Series 80, 29–39.

Thomson, R.E., Mihaly, S.F., Rabinovich, A.B., McDuff, R.E., Scott, R.V., Stahr, F.R., 2003. Constrained circulation at Endeavour ridge facilitates colonization by vent larvae. Nature 424, 545–549.

Thomson, R.E., Roth, S.E., Dymond, J., 1990. Near-inertial motions over a mid-ocean ridge: effects of topography and hydrothermal plumes. Journal of Geophysical Research 95, 12,961–12,966.

Thurnherr, A.M., Ledwell, J.R. and Lavelle, J.W., Regional circulation near the crest of the East Pacific Rise between 9° and 10°N. Deep-Sea Research I, submitted.

Tyler, P.A., Young, C.M., 1999. Reproduction and dispersal at vents and cold seeps. Journal of the Marine Biological Association of the United Kingdom 79, 193–208.

Werner, F.E., Page, F.H., Lynch, D.R., Loder, J.W., Lough, R.G., Perry, R.I., Greenberg, R.M., Sinclair, M.M., 1993. Influences of mean advection and simple behavior on the distribution of cod and haddock early life stages on Georges Bank. Fisheries Oceanography 2 (2), 43–64.

Wilcock, W.S.D., Toomey, D.R., Purdy, G.M., Solomon, S.C., 1993. The renavigation of Sea Beam bathymetric data between 9°N and 10°N on the East Pacific Rise. Marine Geophysical Researches 15, 1–12.

Young, C.M., Chia, F.S., 1987. Abundance and distribution of pelagic larvae as influenced by predation, behavior and hydrographic factors. In: Giese, A.C., Pearse, J.S., Pearse, V.B. (Eds.), Reproduction of Marine Invertebrates, IX, General Aspects: Seeking Unity in Diversity. Blackwell Scientific and The Boxwood Press, Palo Alto and Pacific Grove, CA, pp. 385–463.